Incremental fault-tolerant control for a hybrid quad-plane UAV subjected to a complete rotor loss

Wang, Xuerui; Sun, Sihao

DOI
10.1016/j.ast.2021.107105

Publication date
2021

Document Version
Final published version

Published in
Aerospace Science and Technology

Aerospace Science and Technology 125 (2022) 107105

Contents lists available at ScienceDirect

Aerospace Science and Technology

www.elsevier.com/locate/aescte

Incremental fault-tolerant control for a hybrid quad-plane UAV subjected to a complete rotor loss

Xuerui Wang *, Sihao Sun

Faculty of Aerospace Engineering, Delft University of Technology, Kluyverweg 1, 2629HS Delft, the Netherlands

ARTICLE INFO

Article history:
Received 4 June 2021
Received in revised form 8 August 2021
Accepted 6 September 2021
Available online 13 September 2021
Communicated by Damiano Casalino

Keywords:
Quad-plane
Fault-tolerant control
Aerodynamic modeling
Adaptive sliding mode control
Incremental nonlinear control

ABSTRACT

Quad-plane is a popular type of electric vertical and takeoff/landing (eVTOL) vehicle that hybridizes a quadrotor and a fixed-wing airplane. However, the mechanical simplicity of a quad-plane also makes it vulnerable to rotor failures. When a complete rotor fails, it becomes physically impossible to stop the quad-plane from fast yaw spinning, which further induces considerable abnormal aerodynamic forces and moments on the wing. In this paper, a novel incremental adaptive sliding mode control (I-ASMC) is proposed to address these challenges. First, by exploiting sensor measurements, it simultaneously reduces the control model dependency and the minimum possible sliding mode control/observer gains. Second, finite-time convergence is guaranteed in the Lyapunov sense. Third, the control gains are automatically adapted to their minimum possible values without prior-knowledge on the uncertainty bounds. The proposed I-ASMC method is verified on a high fidelity simulation platform with computational fluid dynamic (CFD) aerodynamic models. Simulation results demonstrate that I-ASMC can drive a quad-plane with a complete loss of a single rotor to follow a trajectory. Its robustness to aerodynamic model uncertainties and rotor faults is also better than the linear quadratic regulator (LQR) and the incremental nonlinear dynamic inversion (INDI) control. In conclusion, the reduced model dependency, implementation simplicity, and improved robustness make the proposed I-ASMC promising for enhancing quad-plane safety in real life.

1. Introduction

Multi-rotor aerial vehicles are widely used nowadays, in applications such as drone delivery, inspections, agriculture, and even for future aerial transportation in the urban area. Among various types of multi-rotor aerial vehicles, quad-planes (Fig. 1) are widely used thanks to their structural simplicity and high aerodynamic efficiency. A quad-plane has two operating configurations. During the vertical take-off/landing and hovering phases, it operates like a quadrotor. During level flights, the four rotors stop rotating, and the quad-plane flies like a fixed-wing aircraft: uses wing(s) to generate lift and uses forward-facing propeller(s) to generate thrust.

The same as a quadrotor, a quad-plane is prone to crash if the complete failure of a rotor happens during the hovering phase because it lacks rotor redundancies. Fault-tolerant control (FTC) is a promising solution for rotor failures. However, FTC is physically incapable of stopping the faulty quad-plane from fast yaw spinning. The reason is explained as follows. Rotors of a quad-plane spin in opposite directions to make use of their reaction torques for heading control. Rotors diagonally across from each other spin in the same direction, to prevent yawing during pitching and rolling maneuvers. However, when a single rotor fails, another rotor on the diagonally opposite side needs to stop or reduce its thrust to prevent the vehicle from tipping over. As a consequence, the other two remaining rotors spinning in the same direction will generate most of the lift, which also produces a considerate amount of unbalanced yaw torque, leading to inevitable spinning motions.

The FTC problems for a quadrotor with complete loss of single or even double rotors have been addressed in the literature [2–9]. Differently from a quadrotor, the large wing of a quad-plane can generate considerable aerodynamic forces and moments during the fast-spinning motions. It is challenging to model these aerodynamic effects because on one side of the quad-plane, the upstream flow can even blow from the trailing edge to the leading edge of the wing. This can induce local flow separations and intensify the

* Corresponding author.
E-mail addresses: X.Wang-6@tudelft.nl (X. Wang), S.Sun-4@tudelft.nl (S. Sun).

https://doi.org/10.1016/j.ast.2021.107105

Fig. 1. A quad-plane example: Avy for medical delivery [1].

unsteadiness of the flow. If a controller relies on an accurate aerodynamic model, computational fluid dynamics analysis needs to be conducted for all the flow conditions, which is costly. Therefore, an FTC design that stabilizes the faulty spinning quad-plane and is robust to aerodynamic uncertainties is desirable. In the literature, the incremental nonlinear dynamic inversion (INDI) control method has been applied to quadrotor FTC problems considering external disturbances [10]. INDI is a sensor-based control method, which enhances control robustness by exploiting the sensor measurements.

Although INDI has shown promising effectiveness in quadrotor FTC problems and may also be capable in quad-plane FTC problems, its resulting closed-loop dynamics are still perturbed by bounded residual uncertainties. To solve this issue, the incremental sliding mode control driven by sliding mode disturbance observer was proposed in [11]. On the one hand, the residual uncertainties are observed and compensated for. On the other hand, the sensor-based incremental control framework reduces the minimum possible sliding mode control and observer gains. The method proposed in [11] has been further improved in [4], where both nonlinear sliding surface and nonlinear reaching laws have been designed for guaranteeing finite-time convergence. However, the method in [4] is only applicable for systems whose relative degrees are equal to two. In view of this, an incremental control scheme that is able to achieve higher-order sliding modes was proposed in [12]. Its stability in the presence of model uncertainties and external disturbances is guaranteed in the Lyapunov sense.

As compared to the mainstream model-based higher-order sliding mode control methods, the sensor-based incremental sliding mode control reduces the residual uncertainties in sliding variable dynamics in spite of its reduced model dependency. Nevertheless, the sliding variable stabilization still assumes known knowledge of the uncertainty upper bound. In practice, uncertainties are normally time-varying, thus it is meaningful to adapt the sliding mode control/observer gains such that they are as small as possible, but are still sufficient to maintain sliding modes. To this end, a novel dual-layer nested adaptive structure was proposed in [13]. However, the input of the first-order scheme is discontinuous, while the second-order super-twisting scheme only adapts one of the gains under the assumption that the other gain is sufficiently large. This adaptive structure was further improved in [14], in which all the super-twisting gains are adapted without prior knowledge of the uncertainty bound.

To the best of the authors' knowledge, this paper presents the first nonlinear fault-tolerant controller for a quad-plane with complete loss of a single rotor. A novel control method named incremental adaptive sliding mode control (I-ASMC) is first proposed in this paper, which has the following features: 1) it simultaneously reduces the model dependency of the controller and the residual uncertainties in the sliding variable dynamics; 2) the residual uncertainties are observed and compensated for in finite time; 3) on the sliding surface, the convergence time to the equilibrium is finite; 4) the sliding mode disturbance observer gains are adapted without requiring information about the bounds on uncertainties and their derivatives; 5) the virtual control is allocated optimally considering actuator position and rate limits.

The first feature of I-ASMC is enabled by the senor-based control structure of incremental control, thus it also holds in the conventional INDI control. By exploiting the sensor measurements, INDI naturally has certain robustness against faults. However, INDI does not have the rest four features of I-ASMC, which can lead to the worse performance of INDI in the presence of faults.

This paper is organized as follows. The quad-plane dynamics are presented in Sec. 2. The nonlinear fault-tolerant control is proposed in Sec. 3. The effectiveness of this controller is demonstrated in Sec. 4 with main conclusions drawn in Sec. 5.

2. Dynamic modeling

The quad-plane considered in this paper is shown in Fig. 2, which has four rotors and one pushing propeller (not used during hovering). The wing of the quad-plane is assumed to be rigid. The following right-handed reference frames are defined and shown in Fig. 2:

- Inertia Frame: $\mathcal{F}_I$ (O_I, x_I, y_I, z_I). Under the assumption that the Earth is flat and non-rotating, the Earth-center Earth-fixed reference frame can be used as an inertia frame.
- Body-fixed Reference Frame: $\mathcal{F}_B$ (O_b, x_b, y_b, z_b). O_b is selected at the center of mass of the quad-plane. $O_b x_b$ and $O_b z_b$ are defined in the symmetrical plane. Moreover, $O_b x_b y_b$ is parallel to the four-rotor planes.
- Local Airfoil Reference Frame: $\mathcal{F}_{a_i}$ $(O_{a_i}, x_{a_i}, y_{a_i}, z_{a_i})$. O_{a_i} is located at the aerodynamic center of the i-th strip. $O_{a_i} x_{a_i}$ is aligned with the chord, pointing towards the trailing edge. $O_{a_i} y_{a_i}$ is perpendicular to $O_{a_i} x_{a_i}$, pointing towards the upper surface.

In this paper, bold symbols indicate vectors and matrices. $\boldsymbol{R}_{ij}$ is used to denote the direction cosine matrix from the reference frame $\mathcal{F}_j$ to the reference frame $\mathcal{F}_i$. The superscript $(\cdot)^k$ indicates expressing the vector $(\cdot)$ in the reference frame $\mathcal{F}_k$. In addition, $\tilde{(\cdot)}$ denotes the skew symmetric matrix of the vector $(\cdot)$. $\boldsymbol{I}_{n\times n}$ denotes a n dimensional identity matrix.

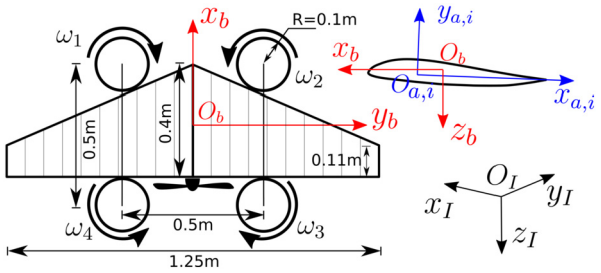

Fig. 2. Geometric properties and coordinate frame definitions of the quad-plane model.

2.1. Quadplane dynamic model

The kinematics and dynamics of a quad-plane are

$$\ddot{\boldsymbol{\xi}}^I = \dot{\boldsymbol{V}}^I = \boldsymbol{g}^I + \boldsymbol{R}_{IB}(\boldsymbol{F}_r^B + \boldsymbol{F}_w^B)/m \tag{1}$$

$$\dot{\boldsymbol{R}}_{IB} = \boldsymbol{R}_{IB}\tilde{\boldsymbol{\omega}}^B \tag{2}$$

$$\boldsymbol{I}_v^B\dot{\boldsymbol{\omega}}^B = -\tilde{\boldsymbol{\omega}}^B\boldsymbol{I}_v^B\boldsymbol{\omega}^B + \boldsymbol{M}_r^B + \boldsymbol{M}_w^B + \boldsymbol{M}_g^B \tag{3}$$

where $\boldsymbol{\xi}^I = [x,\ y,\ z]^\mathsf{T}$ and $\boldsymbol{V}^I = [v_x,\ v_y,\ v_z]^\mathsf{T}$ are quad-plane position and velocity vectors expressed in $\mathcal{F}_I$, respectively. The angular velocity of $\mathcal{F}_B$ with respect to $\mathcal{F}_I$, expressed in $\mathcal{F}_B$ is $\boldsymbol{\omega}^B = [\omega_x,\ \omega_y,\ \omega_z]^\mathsf{T}$. The quad-plane total mass and inertia are denoted by m and $\boldsymbol{I_v}^B$, respectively. $\boldsymbol{g}^I$ denotes the gravitational acceleration vector. $\boldsymbol{F}_r^B$ and $\boldsymbol{M}_r^B$ represent the rotor-generated force and moment, respectively; $\boldsymbol{F}_w^B$ and $\boldsymbol{M}_w^B$ represent the force and moment caused by the wing, respectively. $\boldsymbol{M}_g^B$ indicates the rotor-induced gyroscopic moment [2].

2.2. Quad-plane aerodynamic model

This section establishes the quad-plane aerodynamic model. It is noteworthy that INDI and the proposed I-ASMC do not know anything about the wing-induced aerodynamics; they only need the control effectiveness of the rotors. This will be further elaborated in Sec. 3.2.1.

2.2.1. Wing-induced aerodynamics

The aerodynamic effects of the wing are modeled using the quasi-steady strip theory. As shown in Fig. 2, the wing is discretized into $n = 20$ undeformable strips; each one of the strips, indexed by i, is attached with a local airfoil reference frame $\mathcal{F}_{a_i}$ $(O_{a_i}, x_{a_i}, y_{a_i}, z_{a_i})$. Denote the distance vector from O_b to O_{a_i}, expressed in $\mathcal{F}_B$ as $\boldsymbol{r}_{a_i,b}^B$, then the absolute velocity of O_{a_i}, expressed in $\mathcal{F}_{a_i}$ is calculated as

$$\boldsymbol{V}_{a_i}^{a_i} = [V_{x,a_i}, V_{y,a_i}, V_{z,a_i}]^\mathsf{T} = \boldsymbol{R}_{a_iB}(\boldsymbol{R}_{BI}\boldsymbol{V}^I + \tilde{\boldsymbol{\omega}}^B\boldsymbol{r}_{a_i,b}^B) \tag{4}$$

It is noteworthy that flight dynamics and aerodynamics have different conventions: the former lets the airfoil move in the static air, while the latter anchors the airfoil and lets the flow blows towards the airfoil. Consequently, when observing in the local airfoil reference frame, the incoming flow speed vector actually equals $-\boldsymbol{V}_{a_i}^{a_i}$. In nominal conditions, $V_{x,a_i} < 0$, which indicates that the flow travels from the leading-edge direction towards the trailing-edge direction. However, when a rotor of a quad-plane fails completely, the quad-plane starts to spin. Therefore, it becomes possible that the flow blows from the trailing-edge direction, i.e., $V_{x,a_i} > 0$. In spite of the sign of V_{x,a_i}, define the local dynamic pressure and angle of attack as follows:

$$q_{\infty,i} = 0.5\rho(\boldsymbol{V}_{a_i}^{a_i})^\mathsf{T}\boldsymbol{V}_{a_i}^{a_i}, \quad \alpha_i = -\arcsin\left(V_{y,a_i}/\|\boldsymbol{V}_{a_i}^{a_i}\|_2\right) \tag{5}$$

where ρ is the air density. The singularity at $V_{x,a_i} = 0$ is avoided by the definition of α_i in Eq. (5). In this paper, the airfoil of the quad-plane is selected as NACA 24112. Using the computational fluid dynamics (CFD), the airfoil pressure distributions with constant $\|\boldsymbol{V}_{a_i}^{a_i}\|_2 = 3$ m/s and various $\boldsymbol{V}_{a_i}^{a_i}$ directions are shown in Fig. 3. Furthermore, the resulting aerodynamic coefficients are illustrated in Fig. 4.

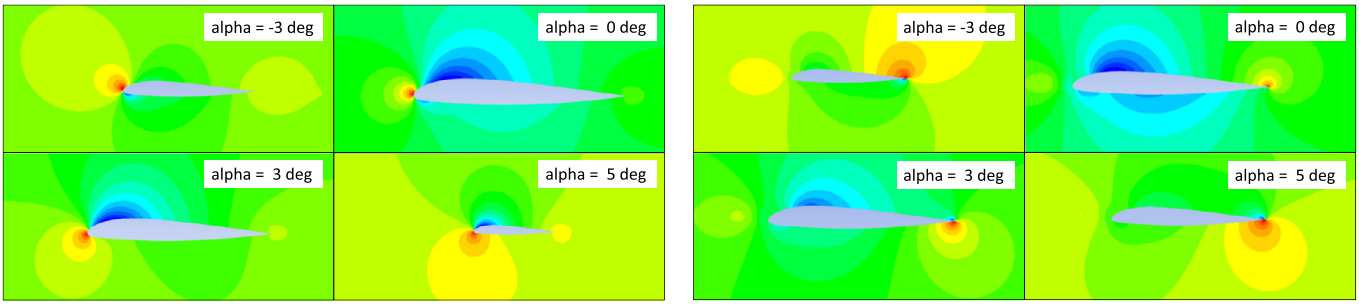

(a) Flow comes from the leading edge ($V_{x,a_i} < 0$). (b) Flow comes from the trailing edge ($V_{x,a_i} > 0$).

Fig. 3. CFD results for the pressure distributions of a single wing strip.

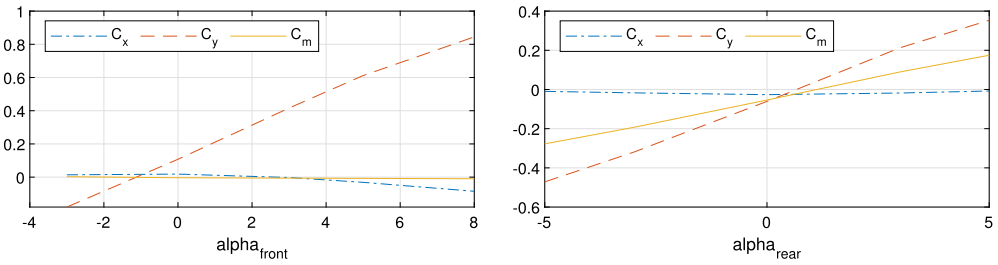

(a) Flow from the leading edge ($V_{x,a_i} < 0$). (b) Flow from the trailing edge ($V_{x,a_i} > 0$).

Fig. 4. CFD results for the three-axes aerodynamic coefficients of a single wing strip.

During flight dynamic simulations, based on the sign of V_{x,a_i}, the local aerodynamic coefficients are interpolated from either Fig. 4a or Fig. 4b. To consider the downwash effects caused by wingtip vortices, the resulting coefficients are multiplied with a local scaling factor $k_{\text{vo},i}$. This factor equals one for the root strip and elliptically reduces to zero towards the wingtip. The local aerodynamic force and moment expressed in $\mathcal{F}_{a_i}$ are $\boldsymbol{f}_{a_i}^{a_i} = q_{\infty,i} S_i \cdot [C_{x,i}, C_{y,i}, 0]^\mathsf{T}$ and $\boldsymbol{m}_{a_i}^{a_i} = q_{\infty,i} S_i c_i \cdot [0, C_{m,i}, 0]^\mathsf{T}$, where $C_{x,i}, C_{y,i}, C_{m,i}$ are the aerodynamic coefficients; S_i and c_i respectively denote the local strip area and chord. Finally, the distributed forces and moments are integrated in the body reference frame, leading to total aerodynamic force and moment, expressed in $\mathcal{F}_B$ as

$$\boldsymbol{F}_w^B = \sum_{i=1}^{n} \boldsymbol{R}_{Ba_i} \boldsymbol{f}_{a_i}^{a_i}, \quad \boldsymbol{M}_w^B = \sum_{i=1}^{n} \boldsymbol{R}_{Ba_i} \boldsymbol{m}_{a_i}^{a_i} + \sum_{i=1}^{n} \tilde{\boldsymbol{r}}_{a_i,b}^B (\boldsymbol{R}_{Ba_i} \boldsymbol{f}_{a_i}^{a_i}) \tag{6}$$

2.2.2. Rotor-induced aerodynamics

The rotor-induced aerodynamic model considers the thrust, drag torque, and in-plane forces and moments. For a rotor indexed by j, use $\boldsymbol{F}_{r,j}^B = [F_{r,j,x},\ F_{r,j,y},\ F_{r,j,z}]^\mathsf{T}$ and $\boldsymbol{M}_{r,j}^B = [M_{r,j,x},\ M_{r,j,y},\ M_{r,j,z}]^\mathsf{T}$ to represent the rotor-induced forces and moments expressed in $\mathcal{F}_B$. Specifically, the thrust and drag toque are expressed as

$$F_{r,j,z} = -C_t(\mu_j, \alpha_j, \boldsymbol{k_t}) \rho \pi \omega_j^2 R^4, \quad M_{r,j,z} = s_j C_q(\mu_j, \alpha_j, \boldsymbol{k_q}) \rho \pi \omega_j^2 R^5 \tag{7}$$

where ω_j is the angular rate of the j-th rotor, R is the rotor radius, $s_j \in \{-1,\ 1\}$ indicates the rotor rotation direction (1 for counter-clockwise). C_t and C_q are thrust and torque coefficients. They are expressed as 2-D polynomial functions parameterized by $\boldsymbol{k}_t$ and $\boldsymbol{k}_q$, respectively. The inputs of C_t and C_q, namely the rotor advance-ratio μ_j and the angle-of-attack α_j, are defined as

$$\mu_j = \|\boldsymbol{V}_j^B\|_2 / (\omega_i R), \quad \alpha_j = \arcsin\left(V_{z,j} / \|\boldsymbol{V}_j^B\|_2\right) \tag{8}$$

where the local velocity of each rotor is defined as

$$\boldsymbol{V}_j^B = [V_{x,j},\ V_{y,j},\ V_{z,j}]^\mathsf{T} = \boldsymbol{R}_{BI} \boldsymbol{V}^I + \tilde{\boldsymbol{\omega}}^B \boldsymbol{r}_j^B \tag{9}$$

where $\boldsymbol{r}_j^B = [r_{j,x},\ r_{j,y},\ r_{j,z}]^\mathsf{T}$ is the distance vector from O_b to the hub of the j-th rotor, expressed in $\mathcal{F}_B$.

The in-plane forces and moments of the j-th rotor are established as parametric models:

$$\begin{aligned} [F_{r,j,x},\ F_{r,j,y}] &= [k_1 V_{x,j}\omega_j + k_2 s_j V_{y,j}\omega_j,\ \ k_1 V_{y,j}\omega_j - k_2 s_j V_{x,j}\omega_j] \\ [M_{r,j,x},\ M_{r,j,y}] &= [-k_3 V_{y,j}\omega_j + k_4 s_j V_{x,j}\omega_j,\ \ k_3 V_{x,j}\omega_j + k_4 s_j V_{y,j}\omega_j] \end{aligned} \tag{10}$$

where k_1 to k_4 are parameters identified from flight data. In this paper, the values of k_1 to k_4, $\boldsymbol{k}_t$ and $\boldsymbol{k}_q$, are the same as parameters in Ref. [15]. Finally, the rotor-induced aerodynamic force and moment vectors are $\boldsymbol{F}_r^B = \sum_{j=1}^4 \boldsymbol{F}_{r,j}^B$, $\boldsymbol{M}_r^B = \sum_{j=1}^4 (\boldsymbol{M}_{r,j}^B + \tilde{\boldsymbol{r}}_j^B \boldsymbol{F}_j^B)$.

3. Control design

3.1. Quad-plane reduced attitude control

As discussed in the preceding sections, a quad-plane inevitably spins when one rotor fails. Therefore, the reduced attitude control which relinquishes the heading control is adopted. To this end, the full kinematic model in Eq. (2) is replaced by the reduced attitude kinematic model [10]:

$$\dot{\boldsymbol{n}}^B = \tilde{\boldsymbol{n}}^B \boldsymbol{\omega}^B + \boldsymbol{R}_{BI} \dot{\boldsymbol{n}}^I, \tag{11}$$

where $\boldsymbol{n}$ is a unit vector and $\boldsymbol{n}^B = [n_x,\ n_y,\ n_z]^\mathsf{T}$. Specifically, $\boldsymbol{n}$ is selected as the *desired thrust direction*, which is computed as $\boldsymbol{n} = (\boldsymbol{a}_{\text{des}} - \boldsymbol{g}) / (\|(\boldsymbol{a}_{\text{des}} - \boldsymbol{g})\|_2)$. The designed acceleration $\boldsymbol{a}_{\text{des}}$ is provided by an outer-loop proportional-integral-derivative (PID) position controller:

$$\boldsymbol{a}_{\text{des}} = \boldsymbol{K}_p \left(\boldsymbol{\xi}_{\text{ref}} - \boldsymbol{\xi}\right) + \boldsymbol{K}_d \left(\dot{\boldsymbol{\xi}}_{\text{ref}} - \dot{\boldsymbol{\xi}}\right) + \boldsymbol{K}_I \int \left(\boldsymbol{\xi}_{\text{ref}} - \boldsymbol{\xi}\right) \mathrm{d}t \tag{12}$$

where $\boldsymbol{K}_p$, $\boldsymbol{K}_d$, $\boldsymbol{K}_I$ are positive diagonal gain matrices.

The reduced attitude control strategy then aligns a body-fixed vector $\boldsymbol{n}_{\text{ref}}^B = [n_{\text{ref},x},\ n_{\text{ref},y},\ n_{\text{ref},z}]^\mathsf{T}$ with $\boldsymbol{n}^B$. A most straightforward choice of the body-fixed unit vector $\boldsymbol{n}_{\text{ref}}^B$ is the thrust direction, namely $\boldsymbol{n}_{\text{ref}}^B = [0,\ 0,\ -1]^\mathsf{T}$. As such, the quadrotor spins flatly, and the rotor diagonally opposite to the damaged rotor does not produce any thrust. In other word, this rotor is saturated at its minimum value (zero), which is unfavourable for control purposes. Therefore, we select $\boldsymbol{n}_{\text{ref}}^B$ slightly (10 to 15 deg) tilting towards the rotor that is diagonally opposite to the damaged rotor, such that it needs to produce a certain amount of thrust to maintain hovering, and its lower saturation can be circumvented. We recommend the readers to [16] for detailed analyses regarding the selection of $\boldsymbol{n}_{\text{ref}}^B$. Since both $\boldsymbol{n}_{\text{ref}}$ and $\boldsymbol{n}$ are unit vectors, projecting them on $\mathcal{F}_B$ and minimizing the differences of their first two components $[n_x - n_{\text{ref},x},\ n_y - n_{\text{ref},y}]$ are sufficient for driving $\boldsymbol{n}$ towards $\boldsymbol{n}_{\text{ref}}$.

Based on the proceeding discussions, define the controlled variables as $\boldsymbol{y} = [z,\ n_x,\ n_y]^\mathsf{T}$ and its reference as $\boldsymbol{y}_{\text{ref}} = [z_{\text{ref}},\ n_{\text{ref},x},\ n_{\text{ref},y}]$. The control input vector is defined as $\boldsymbol{u} = [\omega_1^2,\ \omega_2^2,\ \omega_3^2,\ \omega_4^2]^\mathsf{T}$.

3.2. Incremental adaptive sliding mode control

3.2.1. Incremental control with control allocation

Considering the quad-plane dynamics in Eqs. (1)-(3) as well as the input and output vectors defined in Sec. 3.1, formulate the input-output mapping as follows:

$$\boldsymbol{y}^{(\boldsymbol{r})} = \boldsymbol{\alpha}(\boldsymbol{x}) + \boldsymbol{\mathcal{B}}(\boldsymbol{x})\boldsymbol{u} + \boldsymbol{d}_y \tag{13}$$

where the number of inputs $m = 4$ and the number of outputs $p = 3$. $\boldsymbol{r} = [r_1, r_2, ..., r_p]^\mathsf{T}$ is the vector relative degree of $\boldsymbol{y}$ with respect to $\boldsymbol{u}$. The total state vector is $\boldsymbol{x} \in \mathbb{R}^n$. The external disturbance vector is $\boldsymbol{d}_y \in \mathbb{R}^p$. $\boldsymbol{\alpha}(\boldsymbol{x}) : \mathbb{R}^n \to \mathbb{R}^p$ is the system dynamic vector. $\boldsymbol{\mathcal{B}}(\boldsymbol{x}) : \mathbb{R}^n \to \mathbb{R}^{p\times m}$ is the control effectiveness matrix. In control design, only an estimation of $\boldsymbol{\mathcal{B}}(\boldsymbol{x})$ is implemented.

Specifically, for the selected inputs and outputs, the system relative degree is $\boldsymbol{r} = [2,\ 2,\ 2]^\mathsf{T}$, yielding

$$\boldsymbol{y}^{(\boldsymbol{2})} = \left[\ddot{z},\ \ddot{n}_x,\ \ddot{n}_y\right]^\mathsf{T} = \begin{bmatrix} \sum_{j=1}^4 F_{r,j,z} R_{BI,33}^{-1}/m \\ -\dot{n}_z\omega_y + \dot{n}_y\omega_z - n_z\dot{\omega}_y + n_y\dot{\omega}_z \\ \dot{n}_z\omega_x - \dot{n}_x\omega_z + n_z\dot{\omega}_x - n_x\dot{\omega}_z \end{bmatrix} \tag{14}$$

Substituting Eq. (3) and Eq. (11) into Eq. (14), we have

$$\boldsymbol{y}^{(\boldsymbol{2})} = \boldsymbol{\alpha}(\boldsymbol{x}) + \hat{\boldsymbol{\mathcal{B}}}(\boldsymbol{x})\boldsymbol{u} + \left(\boldsymbol{\mathcal{B}}(\boldsymbol{x}) - \hat{\boldsymbol{\mathcal{B}}}(\boldsymbol{x})\right)\boldsymbol{u} + \boldsymbol{d}_y \tag{15}$$

where

$$\boldsymbol{\alpha}(\boldsymbol{x}) = \begin{bmatrix} 0 \\ (I_z + I_x - I_y)n_y\omega_x\omega_y/I_z + (I_y - I_z + I_x)n_z\omega_x\omega_z/I_y - (\omega_y^2 + \omega_z^2)n_x \\ (I_z - I_x + I_y)n_x\omega_x\omega_y/I_z + (I_x + I_y - I_z)n_z\omega_y\omega_z/I_x - (\omega_x^2 + \omega_y^2)n_y \end{bmatrix} \tag{16}$$

$$\hat{\boldsymbol{\mathcal{B}}}(\boldsymbol{x}) = C_{t,0}\rho\pi R^4 \begin{bmatrix} \boldsymbol{B}_z \\ -n_z\boldsymbol{B}_q + n_y\boldsymbol{B}_r \\ -n_z\boldsymbol{B}_p - n_y\boldsymbol{B}_r \end{bmatrix} \tag{17}$$

with

$$\boldsymbol{B}_z = [-1,\ -1,\ -1,\ -1]/\left(mR_{BI,33}\right) \tag{18}$$

$$\boldsymbol{B}_p = \left[-r_{1,y},\ -r_{2,y},\ -r_{3,y},\ -r_{4,y}\right]/I_x \tag{19}$$

$$\boldsymbol{B}_q = \left[r_{1,x},\ r_{2,x},\ r_{3,x},\ r_{4,x}\right]/I_y \tag{20}$$

$$\boldsymbol{B}_r = [s_1,\ s_2,\ s_3,\ s_4]C_{q,0}/\left(C_{t,0}I_z\right) \tag{21}$$

In Eqs. (14)-(21), s_j, $r_{j,x}$ and $r_{j,y}$ ($j \in \{1,\ 2,\ 3,\ 4\}$) have been defined in Sec. 2.2.2. $R_{BI,33}$ denotes the bottom right entry of $\boldsymbol{R}_{BI}$. I_x, I_y and I_z are the estimated inertia of the quadplane. Note that $\hat{\boldsymbol{\mathcal{B}}}(\boldsymbol{x})$ is an estimation of $\boldsymbol{\mathcal{B}}(\boldsymbol{x})$ by neglecting complex high-speed induced aerodynamic effects introduced in Sec. 2.2. In other words, the coefficients defined in hovering condition, namely $C_{t,0} = C_t(0, 0, \boldsymbol{k}_t)$ and $C_{q,0} = C_q(0, 0, \boldsymbol{k}_q)$, are used in $\boldsymbol{\mathcal{B}}(\boldsymbol{x})$. These coefficients can be identified from the hovering flight data. The usage of $\hat{\boldsymbol{\mathcal{B}}}(\boldsymbol{x})$ instead of $\boldsymbol{\mathcal{B}}(\boldsymbol{x})$ substantially simplifies the control design and implementation processes. Nevertheless, the controller should be robust to the mismatches between $\hat{\boldsymbol{\mathcal{B}}}(\boldsymbol{x})$ and $\boldsymbol{\mathcal{B}}(\boldsymbol{x})$.

The incremental dynamic equation is derived by taking the first-order Taylor series expansion of Eq. (13) around the condition at $t - \Delta t$ (denoted by the subscript 0) as:

$$\boldsymbol{y}^{(\boldsymbol{r})} = \boldsymbol{y}_0^{(\boldsymbol{r})} + \left.\frac{\partial[\boldsymbol{\alpha}(\boldsymbol{x}) + \boldsymbol{\mathcal{B}}(\boldsymbol{x})\boldsymbol{u}]}{\partial\boldsymbol{x}}\right|_0 \Delta\boldsymbol{x} + \boldsymbol{\mathcal{B}}(\boldsymbol{x}_0)\Delta\boldsymbol{u} + \Delta\boldsymbol{d}_y + \boldsymbol{R}_1 \tag{22}$$

in which $\Delta\boldsymbol{x}$, $\Delta\boldsymbol{u}$, and $\Delta\boldsymbol{d}_y$ respectively represents the state, control, and disturbance increments in one sampling time step Δt. $\boldsymbol{R}_1$ is the expansion remainder. Define the output tracking error as $\boldsymbol{e} = \boldsymbol{y} - \boldsymbol{y}_{\text{ref}}$. To stabilize the error dynamics, the control increment is designed to satisfy $\hat{\boldsymbol{\mathcal{B}}}\Delta\boldsymbol{u} = \boldsymbol{v} - \boldsymbol{y}_0^{(\boldsymbol{r})} + \boldsymbol{y}_{\text{ref}}^{(\boldsymbol{r})}$, where $\boldsymbol{v}$ represents the virtual control input. When $\hat{\boldsymbol{\mathcal{B}}}$ is a non-singular square matrix, $\Delta\boldsymbol{u}$ is solved by inverting $\hat{\boldsymbol{\mathcal{B}}}$, leading to the control input of the incremental nonlinear dynamic inversion (INDI) control. In the present paper, $p < m$, thus

the quadratic programming control allocation is adopted, which can also deal with input constrains. The incremental control allocation problem is formulated as follows [17]:

$$\min_{\Delta \boldsymbol{u}} \mathcal{J} = \left((\boldsymbol{y}_0^{(\boldsymbol{r})} - \boldsymbol{\nu} - \boldsymbol{y}_{\text{ref}}^{(\boldsymbol{r})})^{\mathsf{T}} \boldsymbol{W}_1 \hat{\boldsymbol{\mathcal{B}}} + (\boldsymbol{u}_0 - \boldsymbol{u}_*)^{\mathsf{T}} \sigma \boldsymbol{W}_2 \right) \Delta \boldsymbol{u} + \frac{1}{2} \Delta \boldsymbol{u}^{\mathsf{T}} \left(\hat{\boldsymbol{\mathcal{B}}}^{\mathsf{T}} \boldsymbol{W}_1 \hat{\boldsymbol{\mathcal{B}}} + \sigma \boldsymbol{W}_2 \right) \Delta \boldsymbol{u}, \tag{23}$$

$$\text{subject to } \boldsymbol{A}_u \Delta \boldsymbol{u} \leq \boldsymbol{b}_u \tag{24}$$

where $\boldsymbol{W}_1$, $\boldsymbol{W}_2$, σ are weights. $\boldsymbol{u}_*$ is the nominal control, which is set to zero in this problem for saving control energy. $\boldsymbol{A}_u$ and $\boldsymbol{b}_u$ are designed for input constrains [17]. When the j-th rotor fails, the algorithm sets $\boldsymbol{u}_{\min,j} = \boldsymbol{u}_{\max,j} = 0$. Denote the control allocation error as $\boldsymbol{\varepsilon}_{\text{ca}} = \hat{\boldsymbol{\mathcal{B}}} \Delta \boldsymbol{u} - (\boldsymbol{\nu} - \boldsymbol{y}_0^{(\boldsymbol{r})} + \boldsymbol{y}_{\text{ref}}^{(\boldsymbol{r})})$; using Eq. (22), the closed-loop error dynamics are:

$$\boldsymbol{e}^{(\boldsymbol{r})} = \boldsymbol{y}^{(\boldsymbol{r})} - \boldsymbol{y}_{\text{ref}}^{(\boldsymbol{r})} = \boldsymbol{\nu} + \boldsymbol{\delta}(\boldsymbol{x}, \Delta t) + (\boldsymbol{\mathcal{B}}(\boldsymbol{x}_0) - \hat{\boldsymbol{\mathcal{B}}}) \Delta \boldsymbol{u} + \boldsymbol{\varepsilon}_{\text{ca}} + \Delta \boldsymbol{d}_y \triangleq \boldsymbol{\nu} + \boldsymbol{\varepsilon}_{\text{indi}} \tag{25}$$

where $\boldsymbol{\delta}(\boldsymbol{x}, \Delta t)$ is the closed-loop value of the $\Delta \boldsymbol{x}$-related variations and the expansion reminder. $\boldsymbol{\varepsilon}_{\text{indi}}$ is the remaining uncertain perturbation term. Assume there exists a $\boldsymbol{K}_{\boldsymbol{\mathcal{B}}}(\boldsymbol{x}_0)$ such that $\boldsymbol{\mathcal{B}}(\boldsymbol{x}_0) = \boldsymbol{K}_{\boldsymbol{\mathcal{B}}}(\boldsymbol{x}_0) \hat{\boldsymbol{\mathcal{B}}}$, then the following theorem holds:

Theorem 1. *[17] When the quadratic programming control allocation is used (Eq. (24)), if $\| \boldsymbol{I} - \boldsymbol{K}_{\boldsymbol{\mathcal{B}}}(\boldsymbol{x}_0) \|_2 \leq \bar{b}' < 1$, and if $\boldsymbol{\delta}(\boldsymbol{x}, \Delta t)$, $\Delta \boldsymbol{d}_y$, and $\boldsymbol{\varepsilon}_{\text{ca}}$ are respectively bounded by $\bar{\delta}$, $\overline{\Delta d}$, and $\bar{\varepsilon}_{\text{ca}}$, then under sufficiently high sampling frequency, $\boldsymbol{\varepsilon}_{\text{indi}}$ in Eq. (25) is ultimately bounded.*

Essentially, this theorem presents that when the control effectiveness estimation is close to its true value, while the disturbance increments and control allocation errors are bounded, then the lumped uncertainty term $\boldsymbol{\varepsilon}_{\text{indi}}$ is ultimately bounded.

3.2.2. Nominal virtual control design

The nominal virtual control is designed for stabilizing the nominal error dynamics: $\boldsymbol{e}^{(\boldsymbol{r})} = \boldsymbol{\nu}$, which assumes $\boldsymbol{\varepsilon}_{\text{indi}} = \boldsymbol{0}$. The INDI control designs $\boldsymbol{\nu} = -\boldsymbol{K}_{r-1} \boldsymbol{e}^{(\boldsymbol{r-1})} - \boldsymbol{K}_{r-2} \boldsymbol{e}^{(\boldsymbol{r-2})} \ldots - \boldsymbol{K}_0 \boldsymbol{e}$. This design has two issues: first, $\boldsymbol{\varepsilon}_{\text{indi}}$ is not compensated for, thus $\boldsymbol{e}$ can only be ultimately bounded; second, even if $\boldsymbol{\varepsilon}_{\text{indi}} = \boldsymbol{0}$, $\boldsymbol{e}$ only converges asymptomatically instead of in finite time.

To solve these two issues, the incremental adaptive sliding mode control (I-ASMC) is proposed in this paper. Different from INDI, the virtual control is designed as a summation of a sliding mode nominal virtual control $\boldsymbol{\nu}_n$ and a robustify virtual control $\boldsymbol{\nu}_s$.

Proposition 1. *[12] Consider the unperturbed integrator chain set $\boldsymbol{e}^{(\boldsymbol{r})} = \boldsymbol{\nu}_n$, there exists $\epsilon_i \in (0, 1),\ i = 1, \ldots, p$, such that for every $\alpha_i \in (1 - \epsilon_i, 1)$, $\boldsymbol{e}^{(\boldsymbol{r-1})} = \boldsymbol{e}^{(\boldsymbol{r-2})} = \ldots = \boldsymbol{e} = \boldsymbol{0}$ is established in finite time by*

$$\begin{aligned} &\boldsymbol{\nu}_n = [\nu_{n,1}, \nu_{n,2}, \ldots, \nu_{n,p}]^{\mathsf{T}} \\ &\nu_{n,i} = -K_{r-1,i} |e_i^{(r_i-1)}|^{\alpha_{r_i,i}} \text{sign}(e_i^{(r_i-1)}) - K_{0,i} |e_i|^{\alpha_{1,i}} \text{sign}(e_i),\ \ i = 1, \ldots, p \end{aligned} \tag{26}$$

where the gains are chosen such that the r_i^{th}- order polynomials $q^{r_i} + K_{r-1,i} q^{r_i - 1} + K_{r-2,i} q^{r_i - 2} \ldots + K_{0,i}$ are Hurwitz. The scalars $\alpha_{1,i}, \ldots, \alpha_{r_i,i}$ satisfy

$$\alpha_{k-1,i} = \frac{\alpha_{k,i} \alpha_{k+1,i}}{2\alpha_{k+1,i} - \alpha_{k,i}},\ k = 2, \ldots, r_i,\ i = 1, \ldots, p \tag{27}$$

with $\alpha_{r_i+1,i} = 1,\ \alpha_{r_i,i} = \alpha_i$.

3.2.3. Robustify virtual control design

The robustify virtual control $\boldsymbol{\nu}_s$ is designed to compensator for the $\boldsymbol{\varepsilon}_{\text{indi}}$ in Eq. (25). Design an auxiliary sliding variable as $\boldsymbol{s} = \boldsymbol{e}^{(\boldsymbol{r-1})} - \int \boldsymbol{\nu}_n$, then using Eq. (25), the sliding variable dynamics are

$$\dot{\boldsymbol{s}} = \boldsymbol{\nu}_s + \boldsymbol{\varepsilon}_{\text{indi}} \tag{28}$$

For stabilizing the dynamics of $\boldsymbol{s}$, design the virtual control term as

$$\boldsymbol{\nu}_s = -\boldsymbol{\lambda} |\boldsymbol{s}|^{1/2} \text{sign}(\boldsymbol{s}) - \boldsymbol{\beta} \int_0^T \text{sign}(\boldsymbol{s}(\tau)) \text{d}\tau + \boldsymbol{\phi}(\boldsymbol{s}, \boldsymbol{L}(t)) \tag{29}$$

where $\boldsymbol{\lambda} = \text{diag}\{\lambda_i\}$, $\boldsymbol{\beta} = \text{diag}\{\beta_i\}$, $i = 1, \ldots, p$, $\boldsymbol{\phi} = [\phi_1, \ldots, \phi_p]^{\mathsf{T}}$, $\boldsymbol{L}(t) = [L_1, \ldots, L_p]^{\mathsf{T}}$. Their elements satisfy $\lambda_i > 0,\ \beta_i > 0,\ L_i > \bar{l}_i > 0$, and the following expressions:

$$\lambda_i = \sqrt{L_i(t)} \bar{\lambda}_i,\ \ \beta_i = L_i(t) \bar{\beta}_i,\ \ \phi_i = -\frac{\dot{L}_i(t)}{L_i(t)} s_i(t) \tag{30}$$

Proposition 2. *Consider the dynamics in Eq. (28) with virtual control input Eq. (29), suppose $\boldsymbol{L}(t)$ is bounded and is chosen such that $L_i(t) > \max\{|\dot{\varepsilon}_{\text{indi},i}|, \bar{l}_i\}$, then $\dot{\boldsymbol{s}} = \boldsymbol{s} = \boldsymbol{0}$ is achieved in finite time if the gains $\bar{\lambda}_i$ and $\bar{\beta}_i$ are chosen as $\bar{\beta}_i > 1$ and $\bar{\lambda}_i = 2\sqrt{2\bar{\beta}_i}$ for all $i = 1, \ldots, p$.*

Proof: In the Proposition 3.1 of Ref. [14], the gains are chosen to satisfy a linear inequality, which is equivalent to the frequency domain constrain $\| \bar{G}(s) \|_\infty = \| 1/(2s^2 + \bar{\lambda}_i s + \bar{\beta}_i) \|_\infty < 1$ (here s is the Laplace variable). This constrain can be met by the choices in Proposition 2. In addition, multi-input/multi-output expressions are used in this paper, because for aerospace applications, the gain choices for each control channel can be very different. Analogous to the proof of Proposition 3.1 in [14], the present Proposition 2 can be proved. □

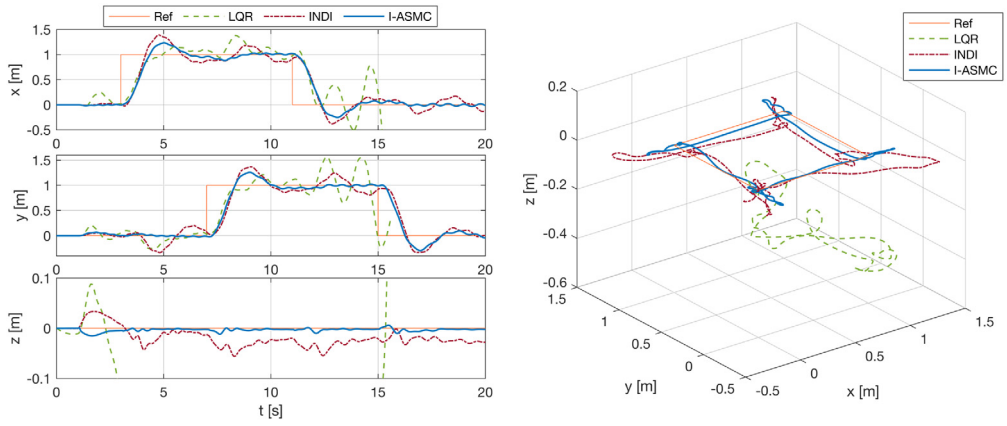

(a) Three-axes trajectory tracking illustration. (b) 3D trajectory tracking illustration.

Fig. 5. Fault-tolerant trajectory tracking comparisons of the proposed three controllers.

The dual-layer adaption scheme [14] is applied to $L_i(t)$ such that it is as small as possible but is still sufficient for maintaining sliding motions. For each $i = 1, ..., p$, define $\delta_i(t) = L_i(t) - (|\bar{u}_{\text{eq}}(t)|/(a_i\bar{\beta}_i) + \kappa_i)$, where $\bar{u}_{\text{eq}}(t)$ equals the low-pass filtered $\beta_i \text{sign}(s_i(t))$. On the sliding surface, $\bar{u}_{\text{eq}}(t)$ presents a real-time estimation of the equivalent control $u_{\text{eq}}(t)$ [14]. The scalar a_i is chosen to satisfy $0 < a_i < 1/\bar{\beta}_i < 1$, and κ_i is a positive scalar chosen to ensure $|\bar{u}_{\text{eq}}(t)|/(a_i\bar{\beta}_i) + \kappa_i/2 > |u_{\text{eq}}(t)|$. The adaption law is given as

$$L_i(t) = \bar{l}_i + l_i(t), \quad \dot{l}_i(t) = -\rho_i(t)\text{sign}(\delta_i(t)), \quad \rho_i(t) = \bar{r}_i + r_i(t), \quad \dot{r}_i(t) = \gamma_i(t)|\delta_i(t)| \tag{31}$$

where $\bar{l}_i$ and $\bar{r}_i$ are small positive scalars for introducing safe margins.

Proposition 3. *Consider the system in Eq. (28) subjects to uncertainty $\boldsymbol{\varepsilon}_{\text{indi}}$, if the first- and second-order time derivatives of $\varepsilon_{\text{indi},i}$ are bounded for $i = 1, ..., p$, then the dual-layer adaption scheme in Eq. (31) ensures $L_i(t) > |\dot{\varepsilon}_{\text{indi},i}|$ in finite time, without requiring the bound information.*

Proof: This can be proved using the Proposition 3.2 in [14]. In addition, a small dead-zone can be applied to the adaptation for attenuating the side effects of measurement noise. □

By far, the derivations and theories of I-ASMC have been completed. As a summary, I-ASMC designs the control increment $\Delta\boldsymbol{u}$, which is solved from the quadratic programming problem formulated in Eq. (24). The designed control increment results in the closed-loop error dynamics in Eq. (25), in which the boundedness of the uncertainty term $\boldsymbol{\varepsilon}_{\text{indi}}$ is ensured in Theorem 1. Given an $\boldsymbol{\varepsilon}_{\text{indi}}$ term with bounded first- and second-order time derivatives, Proposition 3 proves that the dual-layer adaption scheme ensures $L_i(t) > |\dot{\varepsilon}_{\text{indi},i}|$, $i = 1, ..., p$ in finite time. This condition further leads to $\dot{\boldsymbol{s}} = \boldsymbol{s} = \boldsymbol{0}$ in finite time when the remaining conditions in Proposition 2 are also satisfied. According to Eq. (28), $-\boldsymbol{v}_s$ provides a real-time observation of $\boldsymbol{\varepsilon}_{\text{indi}}$ when $\boldsymbol{s} = \boldsymbol{0}$. As a result, the nominal dynamics $\boldsymbol{e}^{(\boldsymbol{r})} = \boldsymbol{v}_n$ are achieved in finite time in spite of uncertainties. Finally, the nominal virtual control designed in Proposition 1 ensures $\boldsymbol{e}^{(\boldsymbol{r}-\boldsymbol{1})} = \boldsymbol{e}^{(\boldsymbol{r}-\boldsymbol{2})} = ... = \boldsymbol{e} = \boldsymbol{0}$ is established in finite time.

The proposed I-ASMC method has reduced model dependency than the widely used model-based sliding mode control (SMC) methods in the literature [4,11]. This is because in Sec. 3.2.1, only the estimated control effectiveness matrix $\hat{\boldsymbol{\mathcal{B}}}$ is used. Even though the model dependency is reduced, the required minimum possible sliding mode control/observer gains are actually also diminished. The main reason is that in Eq. (25), the norm value of the residual error $\boldsymbol{\varepsilon}_{\text{indi}}$ is typically smaller than that of the residual error using model-based SMC methods [4,11].

4. Simulation results

The fault-tolerant performance of the proposed controllers will be numerically evaluated in this section. The geometry property of the tested quad-plane is illustrated in Fig. 2. The moment of inertia is $\boldsymbol{I}_v = \text{diag}\{[0.0027, 0.0027, 0.0052]\}$ kg·m^2, and the quad-plane mass is 1.0 kg. The rotor dynamics are modeled by first-order low-pass filters with time constant $\tau = 0.033$ s. The maximum rotor angular velocity is 1200 rad/s.

Three control methods are compared: INDI, I-ASMC, and a linear quadratic regulator (LQR). The control frequency is 400 Hz. The LQR design and weight selections in this paper are the same as those in [16]. The only model information required by INDI and I-ASMC is the control effectiveness matrix. Also, the quadratic programming control allocation defined in Eq. (24) is used by both INDI and I-ASMC. The weight choices are $\boldsymbol{W}_1 = \boldsymbol{I}_{3\times3}$, $\boldsymbol{W}_2 = \boldsymbol{I}_{4\times4}$, and $\sigma = 0.001$. As discussed in Sec. 3.2.2, the INDI and I-ASMC differs in virtual control design. In this quad-plane fault-tolerant control problem, the relative degree equals $\boldsymbol{r} = [2, 2, 2]^{\text{T}}$, thus the overall INDI virtual control is $\boldsymbol{v} = -\boldsymbol{K}_d\dot{\boldsymbol{e}} - \boldsymbol{K}_p\boldsymbol{e}$, where $\boldsymbol{K}_d = \text{diag}\{[1.6, 12.8, 12.8]\}$ and $\boldsymbol{K}_p = \text{diag}\{[1, 64, 64]\}$. The nominal virtual control of I-ASMC is given in Eqs. (26) and (27). In this specific application, $\nu_{n,1} = -1.6|\dot{e}_1|^{0.80}\text{sign}(\dot{e}_1) - |e_1|^{2/3}\text{sign}(e_1)$, $\nu_{n,2} = -12.8|\dot{e}_2|^{0.80}\text{sign}(\dot{e}_2) - 64|e_2|^{2/3}\text{sign}(e_2)$, $\nu_{n,3} = -12.8|\dot{e}_3|^{0.80}\text{sign}(\dot{e}_3) - 64|e_3|^{2/3}\text{sign}(e_3)$. Note the nominal gains of I-ASMC are chosen to be equal to the gains of INDI for fair comparisons. Moreover, the adaptive sliding mode disturbance observer virtual control is given in Eq. (29). The gain choices are: $\bar{\beta}_1 = 1.1$, $\bar{\beta}_2 = \bar{\beta}_3 = 5.1$, $a_1 = 0.85$, $a_2 = a_3 = 0.18$. The bandwidth of the low-pass filter is chosen as 100 rad/s. In Eq. (31), $\bar{l}_i = 2.1$, $\bar{r}_i = 1.1$, $\kappa_i = 0.1$, $\gamma_i = 1$, for all $i = 1, 2, 3$.

Initially, the quad-plane is hovering with four healthy rotors. Complete failure of rotor #3 occurs at $t = 1$ s (Fig. 2). The references are set as $n_{\text{ref},x} = 0.15$ and $n_{\text{ref},y} = -0.15$ to tilt $\boldsymbol{n}_{\text{ref}}$ towards rotor #1. The primary objective of the controllers is stabilization. As discussed in

Table 1
Tracking performance comparisons between INDI and I-ASMC.

Metrics	rms$(x - x_{\text{ref}})$	rms$(y - y_{\text{ref}})$	rms$(z - z_{\text{ref}})$	rms$(n_x - n_{\text{ref},x})$	rms$(n_y - n_{\text{ref},y})$
INDI	0.2895	0.3065	0.0263	0.0781	0.1190
I-ASMC	0.2692	0.2714	0.0046	0.0434	0.0522
Improvements	7.00 %	11.45 %	82.50 %	44.46 %	56.12 %

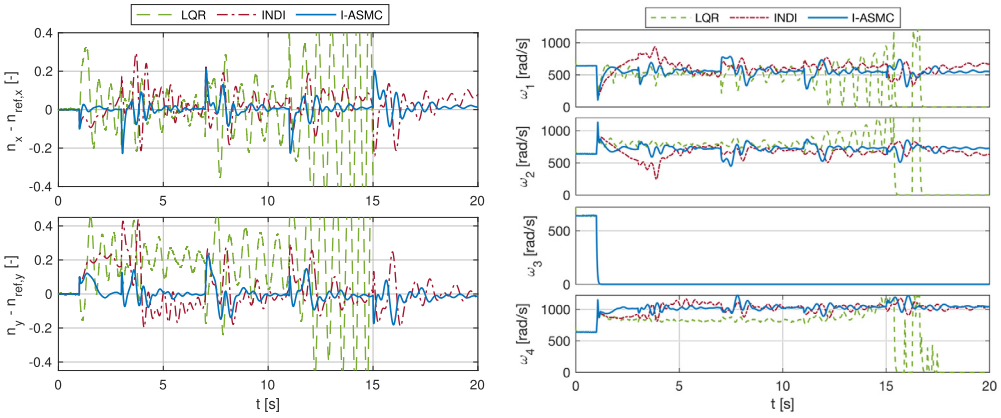

(a) Reduced-attitude tracking errors. (b) Rotor speeds.

Fig. 6. Comparisons of the reduced-attitude tracking errors and rotor speeds of the proposed three controllers.

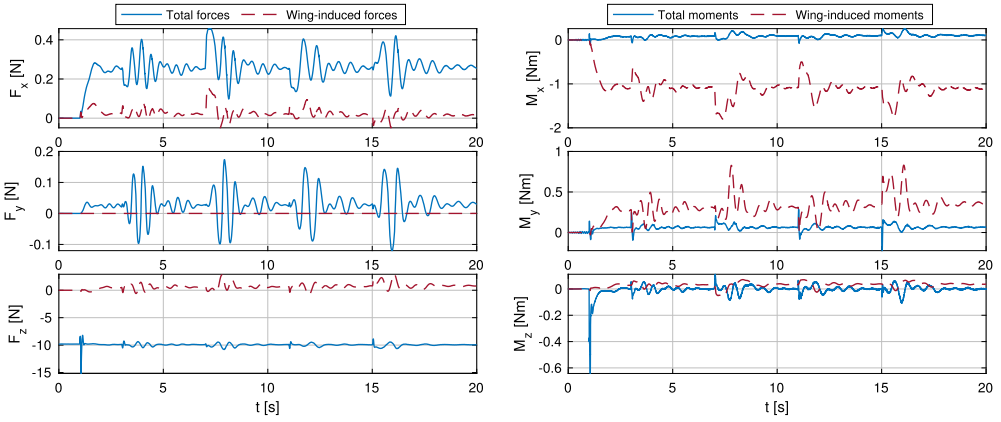

(a) Total and wing-induced forces in $\mathcal{F}_B$. (b) Total and wing-induced moments in $\mathcal{F}_B$.

Fig. 7. Total and wing-induced forces and moments expressed in $\mathcal{F}_B$ (excludes gravity).

Sec. 2.2, it is physically impossible to stop the quad-plane from spinning at low forward flight speed. Furthermore, once it starts spinning, the wing surface would lead to considerable forces and moments, which increase the stabilization difficulties. If the controller is able to stabilize the aircraft, one step further would be taken: way-point tracking.

As shown in Fig. 5, the damaged quad-plane is commanded to track a square trajectory. Even though the LQR controller can stabilize the quad-plane in a few seconds after the rotor failure, the responses deviate from the given commands and eventually results in a crash. On the contrary, both INDI and I-ASMC are able to control the damaged quad-plane to follow the square trajectory. Nevertheless, I-ASMC has better tracking performance. Table 1 summarizes the performance improvement percentages of I-ASMC over INDI.

The reduced-attitude tracking errors and the rotor inputs are illustrated in Fig. 6. After $t = 10$ s, LQR presents oscillatory responses and fails in stabilizing the quad-plane. By contrast, INDI and I-ASMC stabilize the reduced-attitude tracking errors around zero in spite of the rotor failure. The I-ASMC outperforms INDI by over 44% (Table 1) in terms of reduced-attitude tracking accuracy.

The failure of rotor #3 renders the quad-plane yawing around 15 rad/s from $t = 1$ s. Fig. 7 plots the total (excluding gravity) and wing-induced aerodynamic forces and moments. It can be seen that the wing-induced forces are relatively small, as those generated by the left and right wings roughly counteract each other. However, significant wing-induced rolling moments are observed from Fig. 7b. This is because the wing on the advancing side generates positive lift while the retreating side generates negative lift. Considering the difficulties in accurately model the spinning-induced aerodynamics, these effects are kept unknown to the controller. Even so, thanks to their robustness, both INDI and I-ASMC automatically generate more thrust on rotor #4 to compensate for this rolling moment (Fig. 6b). By contrast, the LQR inputs are saturated and eventually lead to the crash.

The sliding mode disturbance observer (SMDO) adaptive gains in the three control channels ($z,\ n_x,\ n_y$) are shown in Fig. 8a. Proposition 3 is verified by Fig. 8a as the gains $L_i(t),\ i = z, n_x, n_y$ are bounded and adapt themselves according to the trend of the uncertainties. According to Proposition 2, this further leads to $\dot{\boldsymbol{s}} = \boldsymbol{s} = \boldsymbol{0}$ in finite time, which is verified in Fig. 8b. Recall Sec. 3.2.3, the responses of

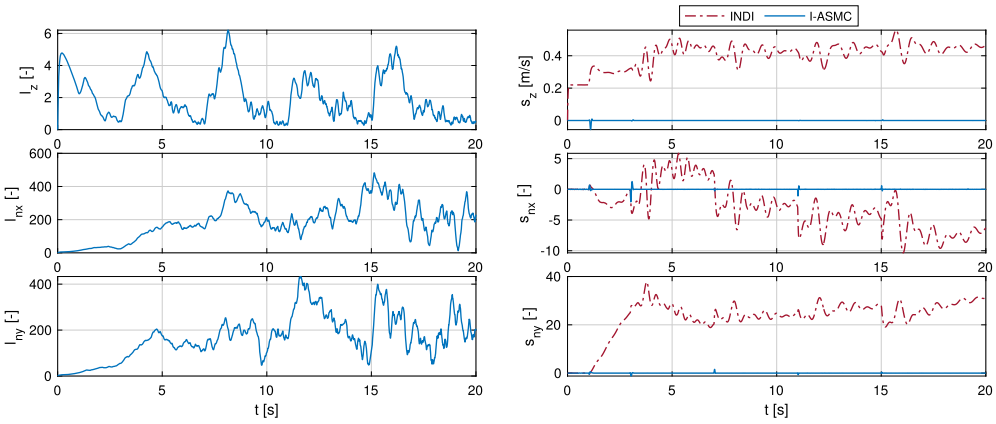

(a) SMDO adaptive gains. (b) Sliding variable comparisons.

Fig. 8. Sliding variable comparisons between INDI and I-ASMC.

$\boldsymbol{s}$ reflect the effects of $\boldsymbol{\epsilon}_{\text{indi}}$ on closed-loop dynamics. Fig. 8b shows that I-ASMC enforces $\boldsymbol{s}$ to zero in finite time, while the remaining perturbations in INDI are not neutralized.

5. Conclusions

This paper presents the first (to the best of the author's knowledge) nonlinear fault-tolerant controller for a quad-plane subjected to a complete loss of a single rotor. Lyapunov-based stability and robustness analyses show that the proposed incremental adaptive sliding mode control (I-ASMC) enforces a generic nonlinear system to equilibrium in finite time, despite model uncertainties, external disturbances, and sudden faults. Moreover, the sliding mode control and observer gains are adapted automatically without knowing the uncertainty bounds. Furthermore, by virtue of its sensor-based control structure, I-ASMC only requires an estimated control effectiveness matrix for implementation, while being robust to the complex aerodynamic uncertainties during the quad-plane fast-spinning motions. Finally, simulation results demonstrate that a linear quadratic regulator (LQR) is insufficient to stabilize a quad-plane with only three rotors. By contrast, the proposed I-ASMC drives the faulty quad-plane to follow a trajectory and shows enhanced robust performance than the incremental nonlinear dynamic inversion control (INDI). Validating I-ASMC by higher fidelity simulations and real-world flight tests are recommended as future work.

Declaration of competing interest

The authors declare that they have no known competing financial interests or personal relationships that could have appeared to influence the work reported in this paper.

References

[1] Avy drones, https://www.avy.eu, 2020.
[2] M.W. Mueller, R. D'Andrea, Stability and control of a quadrocopter despite the complete loss of one, two, or three propellers, in: 2014 IEEE International Conference on Robotics and Automation (ICRA), IEEE, 2014, pp. 45–52.
[3] A. Lanzon, A. Freddi, S. Longhi, Flight control of a quadrotor vehicle subsequent to a rotor failure, J. Guid. Control Dyn. 37 (2) (2014) 580–591.
[4] X. Wang, E. van Kampen, Q. Chu, Quadrotor fault-tolerant incremental nonsingular terminal sliding mode control, Aerosp. Sci. Technol. 95 (2019) 105514, https://doi.org/10.1016/j.ast.2019.105514.
[5] B. Wang, X. Yu, L. Mu, Y. Zhang, A dual adaptive fault-tolerant control for a quadrotor helicopter against actuator faults and model uncertainties without overestimation, Aerosp. Sci. Technol. 99 (2020) 105744, https://doi.org/10.1016/j.ast.2020.105744.
[6] P. Tang, F. Zhang, J. Ye, D. Lin, An integral TSMC-based adaptive fault-tolerant control for quadrotor with external disturbances and parametric uncertainties, Aerosp. Sci. Technol. 109 (2021) 106415, https://doi.org/10.1016/j.ast.2020.106415.
[7] Z. Hou, P. Lu, Z. Tu, Nonsingular terminal sliding mode control for a quadrotor uav with a total rotor failure, Aerosp. Sci. Technol. 98 (2020) 105716.
[8] B. Wang, Y. Shen, Y. Zhang, Active fault-tolerant control for a quadrotor helicopter against actuator faults and model uncertainties, Aerosp. Sci. Technol. 99 (2020) 105745, https://doi.org/10.1016/j.ast.2020.105745.
[9] K. Liu, R. Wang, X. Wang, X. Wang, Anti-saturation adaptive finite-time neural network based fault-tolerant tracking control for a quadrotor uav with external disturbances, Aerosp. Sci. Technol. 115 (2021) 106790, https://doi.org/10.1016/j.ast.2021.106790.
[10] S. Sun, X. Wang, Q. Chu, C. de Visser, Incremental nonlinear fault-tolerant control of a quadrotor with complete loss of two opposing rotors, IEEE Trans. Robot. 37 (1) (2021) 116–130, https://doi.org/10.1109/TRO.2020.3010626.
[11] X. Wang, S. Sun, E. van Kampen, Q. Chu, Quadrotor fault tolerant incremental sliding mode control driven by sliding mode disturbance observers, Aerosp. Sci. Technol. 87 (2019) 417–430, https://doi.org/10.1016/j.ast.2019.03.001.
[12] X. Wang, E. van Kampen, Q. Chu, Comparison of three control structures for inducing higher-order sliding modes, in: 2019 18th European Control Conference (ECC), IEEE, 2019, pp. 4073–4080.
[13] C. Edwards, Y.B. Shtessel, Adaptive continuous higher order sliding mode control, Automatica 65 (March) (2016) 183–190, https://doi.org/10.1016/j.automatica.2015.11.038.
[14] C. Edwards, Y.B. Shtessel, Adaptive dual-layer super-twisting control and observation, Int. J. Control 89 (9) (2016) 1759–1766, https://doi.org/10.1080/00207179.2016.1175030.
[15] S. Sun, C. de Visser, Aerodynamic model identification of a quadrotor subjected to rotor failures in the high-speed flight regime, IEEE Robot. Autom. Lett. 4 (4) (2019) 3868–3875.
[16] M.W. Mueller, R. D'Andrea, Relaxed hover solutions for multicopters: application to algorithmic redundancy and novel vehicles, Int. J. Robot. Res. 35 (8) (2016) 873–889.
[17] X. Wang, T. Mkhoyan, I. Mkhoyan, R. De Breuker, Seamless active morphing wing simultaneous gust and maneuver load alleviation, J. Guid. Control Dyn. 44 (9) (2021), https://doi.org/10.2514/1.G005870, arXiv:2012.14520.